

# Gas-Liquid Simulation of an Airlift Bubble Column Reactor

M. Blažej<sup>a</sup>, G. M. Cartland Glover<sup>b</sup>, S. C. Generalis<sup>b</sup> and J. Markoš<sup>a1</sup>

<sup>a</sup> *Slovak Technical University, Department of Chemical and Biochemical Engineering, Faculty of Chemical and Food Technology, Radlinského 9, Bratislava, 812 37 Slovak Republic.*

<sup>1</sup>corresponding author: *markos@cvt.stuba.sk*

<sup>b</sup> *Aston University, School of Engineering and Applied Science, Division of Chemical Engineering and Applied Chemistry, Birmingham, B4 7ET U. K.*

*S.C.Generalis@aston.ac.uk*

## Keywords:

Airlift reactor (ALR), circulation velocity, gas holdup, CFD, computational fluid dynamics, modelling of hydrodynamics, Fluent.

## Abstract:

The simulation of two-phase flow for an experimental airlift reactor (32-litre volume) using commercially available software from Fluent Incorporated is presented here [1]. Data from the simulation is compared with the experimental data obtained by the tracking of a magnetic particle and analysis of the pressure drop to determine the gas hold-up. Comparisons between vertical velocity and gas hold-up were made for a series of experiments where the superficial gas velocity in the riser was adjusted between 0.01 and 0.075 m s<sup>-1</sup>.

**Introduction:**

The understanding of the complexity of the fluid dynamics in airlift reactors is very important due to their application in the bioprocess industry. Understanding the influence that the hydrodynamics has on biochemical production rates through transport processes such as interphase oxygen transfer, nutrient mixing and the effects of pH. Also of importance is knowledge of the influence of the biomass on the gas phase through inter-phase interactions and the impact the biomass has on the liquid phase viscosity. The fluid mixture becomes a pseudo-plastic fluid as the culture grows and develops, limiting the effectiveness of the transport processes discussed above. In an effort to enhance the performance of equipment over the past two decades many attempts have been made to develop accurate and workable predictive models of the flow regimes present. The work presented here is an initial comparison between simulated data produced using the computational fluid dynamics (CFD) code for two-phase fluid flow developed by FLUENT Inc. and experimental data recorded using the magnetic tracer particle method [2] for a Newtonian liquid in a 32-litre airlift reactor. The simulations presented here follows on from the simulation of a 5:1 bubble column in two dimensions [3], [4].

**Experimental:**

Experimental investigations were performed using a 32-litre concentric draft-tube airlift reactor, with the riser in the draft-tube and the downcomer between the draft tube and outer cylinder (Figure 1). The dimensions of the column are 1.818 m of liquid height, with a 0.147 m column internal diameter.

The gas sparger at the base of the column had a diameter of 0.079 m containing 25 holes that were 0.5 mm in diameter. The draft tube was positioned 0.046 m above the gas sparger with a tube height was 1.710 m with an internal diameter of 0.106 m and an external diameter of 0.118 m (i.e. 6 mm wall thickness). The cross-sectional area ratio between the downcomer and the riser was 0.95, with the liquid height to column diameter ratio at 12:1. The top section is a gas disengager with a diameter of 0.294 m. A series of experiments were performed by varying the superficial gas velocity (with respect to the cross-sectional area of the riser) over the range of 0.005 to 0.075 m s<sup>-1</sup> to create a characteristic velocity curve of the airlift reactor. The gas hold-up in the riser and the downcomers was measured using the inverted U-tube Manometer method as described by Chisti [5]. The signals were measured using A/D convertors and recorded on PC. The fluid velocity in the riser and downcomer was measured using a magnetic particle tracing method [2]. As a magnetic flow tracer was used neutrally buoyant spherical particle (diameter 1 cm). This particle contained a special alloy with a high relative magnetic permeability (over 10 000) embedded in epoxy resin. The transition of the particle (as it passes through measuring points) was measured by an A/D convertor, recorded and processed on a personal computer using special processing software. Signal of passing particle was registered by two solenoid oscillating coils located at a distance of 0.45 m and 1.5 m from the base of the reactor. Basic oscillating frequencies of both the upper and lower coil were very close (but not the same) of about 150 kHz. As the flow tracer passes through one of the coils, it decreases its oscillation frequency. At this time, in spite of the first one, the second coil simultaneously shifts up its frequency. This increases differential frequency- measured signal consequently processed. This change in

signal appears as peaks. To calculate the velocity of the gas-liquid mixture in both the riser and the downcomer, the time difference in the peaks can be used. Because of flow oscillations and sometimes significant radial movement of the particle and its trapping into backflow (especially in the riser), the standard deviation values of measured circulation velocities in each section were high, thus circulation velocity oscillated depending on momentaneous hydrodynamic conditions in the reactor. To eliminate effects discussed above the circulation velocity was estimated from long-time averaged measured values.

### **Simulations:**

The algebraic slip mixture (ASM) model used for the simulations was developed by Manninien et al. [6] and incorporated in Fluent computational fluid dynamics software [1], [7], [8]. This model describes the flow regime as a single-phase pseudo-continuous mixture of the gas and liquid phases. This means that a single set of continuity and momentum equations can be used to model the flow phenomena.

Continuity equation for the mixture phase:

$$\frac{\partial}{\partial t}(\rho_{\text{mix}}) + \frac{\partial}{\partial X_i}(\rho_{\text{mix}} u_{\text{mix},i}) = 0 \quad (1)$$

Momentum equation for the mixture:

$$\begin{aligned} & \frac{\partial}{\partial t}(\rho u_{\text{mix},j}) + \frac{\partial}{\partial X_i}(\rho_{\text{mix}} u_{\text{mix},i} u_{\text{mix},j}) = \\ & - \frac{\partial p}{\partial X_j} + \frac{\partial}{\partial X_j} \mu_{\text{mix}} \left( \frac{\partial}{\partial X_j} (u_{\text{mix},i}) + \frac{\partial}{\partial X_i} (u_{\text{mix},j}) \right) \\ & + \rho_{\text{mix}} g_j + F_j + \frac{\partial}{\partial X_i} \sum_{k=1}^n \alpha_k \rho_k u_{Dk,i} u_{Dk,j} \end{aligned} \quad (2)$$

Where  $\rho_{\text{mix}}$  is mixture density given by:

$$\rho_{\text{mix}} = \sum_{q=1}^n \alpha_q \rho_q \quad (3)$$

and mixture viscosity

$$\mu_{\text{mix}} = \sum_{q=1}^n \alpha_q \mu_q \quad (4)$$

The momentum equation is modified to include interactions between each phase as a drift or slip velocity effect.

Drift velocity:

$$\vec{u}_{D,q} = \vec{u}_q - \vec{u}_{\text{mix}} = \vec{V}_{q,c} - \frac{1}{\rho_q} \sum_{i=1}^{n-1} \alpha_i \rho_i \vec{V}_{i,c} \quad (5)$$

Slip velocity equation:

$$\vec{V}_{q,c} = \vec{u}_q - \vec{u}_c = \frac{(\rho_{\text{mix}} - \rho_q)}{18\mu_c f} \left( \vec{g}_j - \frac{D\vec{u}_{\text{mix}}}{Dt} \right) \quad (6)$$

Where mass averaged velocity:

$$\bar{u}_{\text{mix}} = \frac{\sum_{q=1}^n \alpha_q \rho_q \bar{u}_q}{\rho_{\text{mix}}} \quad (7)$$

and friction factor given by:

$$f = 1 + 0.05 \text{Re}^{0.687} \quad \text{Re} < 1000 \quad (8)$$

$$f = 0.018 \text{Re} \quad \text{Re} \geq 1000 \quad (9)$$

The friction factor is used in the calculation of the slip velocity, which in turn is used in the calculation of the drift, gas, liquid and mixture phase velocities. This factor is used to estimation of drag forces affecting on the dispersed phase as the bubbles rise up through the liquid phase.

Bubble Reynolds number is given by:

$$\text{Re} = \frac{d_q u_{\text{mix}} \rho_c}{\mu_c} \quad (10)$$

where  $\rho_c$  and  $\mu_c$  represents density and dynamic viscosity respectively of the continuous liquid phase.

This effect depends on the volume fraction of the dispersed and continuous phases, which is control by a volume fraction equation.

Volume fraction equation:

$$\frac{\partial}{\partial t} (\alpha_q \rho_q) + \frac{\partial}{\partial X_i} (\alpha_q \rho_q u_{\text{mix},i}) = - \frac{\partial}{\partial X_i} (\alpha_q \rho_q u_{Dq,i}) \quad (11)$$

In addition to the ASM model the Reynolds stress turbulence transport equations are applied to the solution to account for the effects of turbulence vortices that occur between the gas and liquid phases in the airlift reactor. The

transport of turbulent energy is difficult to predict with many unknown and immeasurable parameters that influence the transport of energy, stress and vortices in a turbulent flow. Therefore to capture all these effects requires the use of a complex model, such as the Reynolds stresses turbulence transport model. The model originates from the exact Reynolds stress turbulence transport equation.

Exact transport equation for the transport of Reynolds Stresses:

$$\begin{aligned}
& \underbrace{\frac{\partial}{\partial t}(\overline{\rho u_i u_j})}_{\text{Local time derivative}} + \underbrace{\frac{\partial}{\partial x_r}(\overline{\rho U_r u_i u_j})}_{\text{Convection-C}_{ij}} = \\
& - \underbrace{\frac{\partial}{\partial x_r}[\overline{\rho u_i u_j u_r} + p(\delta_{rj} u_i + \delta_{ir} u_j)]}_{\text{Turbulent Diffusion-D}_{ij}^T} \\
& + \underbrace{\frac{\partial}{\partial x_r} \left[ \mu \frac{\partial}{\partial x_r} (\overline{u_i u_j}) \right]}_{\text{Molecular Diffusion-D}_{ij}^L} - \underbrace{\rho \left( \overline{u_i u_r} \frac{\partial U_j}{\partial x_r} + \overline{u_j u_r} \frac{\partial U_i}{\partial x_r} \right)}_{\text{Stress Production-P}_{ij}} \\
& - \underbrace{\rho \beta (\overline{g_i u_j \theta} + \overline{g_j u_i \theta})}_{\text{Buoyancy Production-G}_{ij}} + \underbrace{p \left( \frac{\partial u_i}{\partial x_j} + \frac{\partial u_j}{\partial x_i} \right)}_{\text{Pressure Strain-}\theta_{ij}} \\
& - \underbrace{2\mu \frac{\partial u_i}{\partial x_r} \frac{\partial u_j}{\partial x_r}}_{\text{Dissipation-}\varepsilon_{ij}} - \underbrace{2\rho \Omega_r (\overline{u_j u_s \varepsilon_{iks}} + \overline{u_i u_s \varepsilon_{jks}})}_{\text{Production by system rotation-A}_{ij}} \tag{12}
\end{aligned}$$

The exact equation has many unknown terms and is employed in a series of equations to enable closure of each of the unknown terms in the exact equation.

Of the various terms in these exact equations, **Convection-C<sub>ij</sub>**, **Molecular**

*Diffusion- $D_{ij}^L$* , *Stress Production- $P_{ij}$*  and *Production by System Rotation- $A_{ij}$*  do not require any modeling. However, *Turbulent Diffusion- $D_{ij}^T$* , *Buoyancy Production- $G_{ij}$* , *Pressure strain- $\theta_{ij}$*  and *Dissipation- $\varepsilon_{ij}$*  need to be modeled to close the equations. The following sections describe the modeling assumptions required to close the equation set. This includes the use of both the k- $\varepsilon$  equations and the inclusion of other effects such as buoyancy, pressure, pressure-strain and any rotation.

Turbulent diffusive transport:

$$\frac{\partial}{\partial x_r} \left[ \overline{\rho u_i u_j u_r} + \overline{p(\delta_{rj} u_i + \delta_{ir} u_j)} \right] = \frac{\partial}{\partial x_r} \left( \frac{\mu_t}{\sigma_k} \frac{\partial}{\partial x_r} (\overline{u_i u_j}) \right) \quad (13)$$

Buoyancy effects:

$$B_{ij} = \rho \beta (\mathbf{g}_i \overline{u_j \theta} + \mathbf{g}_j \overline{u_i \theta}) = \beta \frac{\mu_t}{Pr_t} \left( \mathbf{g}_i \frac{\partial \rho}{\partial x_j} + \mathbf{g}_j \frac{\partial \rho}{\partial x_i} \right) \quad (14)$$

Stress production:

$$P_{ij} = \rho \left( \overline{u_i u_r} \frac{\partial U_j}{\partial x_r} + \overline{u_j u_r} \frac{\partial U_i}{\partial x_r} \right) \quad (15)$$

Pressure-strain term:

$$\phi_{ij} = \overline{p \left( \frac{\partial u_i}{\partial x_j} + \frac{\partial u_j}{\partial x_i} \right)} \quad (16)$$

Decomposition of pressure-strain term:

$$\phi_{ij} = \phi_{ij,1} + \phi_{ij,2} + \phi_{ij}^w \quad (17)$$

Slow pressure-strain term:

$$\phi_{ij,1} = -C_1 \rho \frac{\varepsilon}{k} \left[ \overline{u_i u_j} - \frac{2}{3} \delta_{ij} k \right] \quad (18)$$

Rapid pressure-strain term:

$$\phi_{ij,2} = -C_2 \left[ \begin{aligned} & \left( P_{ij} + F_{ij} + B_{ij} + \frac{\partial}{\partial x_r} (\rho U_r \overline{u_i u_j}) \right) \\ & + \frac{2}{3} \delta_{ij} \left( \frac{1}{2} P_{rr} + \frac{1}{2} B_{rr} - \frac{1}{2} \frac{\partial}{\partial x_r} (\rho U_r \overline{u_r u_r}) \right) \end{aligned} \right] \quad (19)$$

Wall reflection term:

$$\begin{aligned} \phi_{ij}^w = C'_1 \frac{\varepsilon}{k} & \left( \overline{u_r u_s n_r n_s} \delta_{ij} - \frac{3}{2} \overline{u_i u_r n_j n_r} - \frac{3}{2} \overline{u_j u_r n_i n_r} \right) \frac{k^{3/2}}{(C_\mu^{3/4} / \kappa) \mathcal{E} d_w} \\ & C'_2 \left( \phi_{rs,2} n_s n_s \delta_{ij} - \frac{3}{2} \phi_{ir,2} n_j n_r - \frac{3}{2} \phi_{jr,2} n_i n_r \right) \frac{k^{3/2}}{(C_\mu^{3/4} / \kappa) \mathcal{E} d_w} \end{aligned} \quad (20)$$

System rotation effects:

$$A_{ij} = 2\rho \Omega_r \left( \overline{u_j u_s \varepsilon_{iks}} + \overline{u_i u_s \varepsilon_{jks}} \right) \quad (21)$$

The transport equations described here take account of the turbulent interactions between the two fluids in the airlift reactor.

Total derivative for the turbulent kinetic energy:

$$\frac{Dk}{Dt} = \frac{\partial k}{\partial t} + \frac{\partial k u_i}{\partial x_i} \quad (22)$$

Turbulent kinetic energy transport equation:

$$\rho \frac{Dk}{Dt} = \frac{\partial}{\partial x_i} \left[ \left( \mu + \frac{\mu_t}{\sigma_k} \right) \frac{\partial k}{\partial x_i} \right] + G_k + G_b - \rho \varepsilon \quad (23)$$

Total derivative for the rate of dissipation of energy from the turbulent flow:

$$\frac{D\varepsilon}{Dt} = \frac{\partial\varepsilon}{\partial t} + \frac{\partial\varepsilon u}{\partial x_i} \quad (24)$$

Rate of dissipation of energy from turbulent flow, transport equation:

$$\rho \frac{D\varepsilon}{Dt} = \frac{\partial}{\partial x_i} \left( \mu + \frac{\mu_t}{\sigma_\varepsilon} \right) \frac{\partial\varepsilon}{\partial x_i} + C_{1\varepsilon} \frac{\varepsilon}{k} (G_k + C_{3\varepsilon} G_b) - C_{2\varepsilon} \frac{\varepsilon^2}{k} \quad (25)$$

Turbulent viscosity formulation:

$$\mu_t = \rho C_\mu \frac{k^2}{\varepsilon} \quad (26)$$

Figure 2A shows the domain used to represent the 32-litre reactor. This domain contained ~2500 cells in an unstructured format to reduce the number of mesh cells used (to eliminate excessive computation time), where figure 2B and 2C show the configuration of the mesh at the top and bottom of the domain. The mesh from the bottom section extends up the column to the top section, with an even distribution of cells. The number of cells used had to be reduced for the sake of extremely long computation time. Therefore mesh resolution was optimized as a compromise between both the accuracy of results and computation time. There were performed calculations with different mesh resolutions for one gas vertical velocity. The solutions of these simulations were compared. The mesh resolution, which did not influence the final solution more than about 5%, and was calculable in real time, was established as an optimal resolution, used in further simulations. The flow boundary conditions applied to the mixture phase set the vertical gas velocity as 0.018; 0.036; 0.072; 0.090; 0.108 and 0.135 m s<sup>-1</sup>, with respect to the cross-sectional area of the sparger, a gas phase fraction of 1, and the bubble (air)

diameter as 0.005 m. This bubble diameter was calculated as an average value from values given by correlations described by Kastanek [9] for such superficial velocities of input gas and plate distributor as were used in our system. Table 1 displays the corresponding superficial gas velocities for the experimental data, this superficial velocity is obtain with respect to the riser cross-sectional area. The initial conditions applied to the liquid phase, water was stationary ( $0 \text{ m s}^{-1}$  velocity for all vector components) with a free-slip surface over the upper surface of the domain. Gravitational acceleration vector ( $g$ ) was  $[0, -9.81, 0] \text{ m s}^{-2}$ . Time step size was 0.1 seconds for 2000 time steps with the initial time as 0.0 seconds. Density of air and water were  $1.225$  and  $998.2 \text{ kg m}^{-3}$ , respectively. Viscosity of air and water were  $1.7498e^{-5}$  and  $1.003e^{-3} \text{ kg m}^{-1} \text{ s}^{-1}$ , respectively.

The solver specifications for the discretization of the domain involve the following procedures, "body force weighted" for pressure [8], QUICK [10] for momentum, SIMPLEC [11] for the velocity-pressure coupling and a first-order discretization scheme for the volume fraction and unsteady state, turbulent flow models. The under-relaxation factors, which determine how much control each of the equations has in the final solution, were set to 0.3 for the pressure, 0.7 for the momentum with the Reynolds stress turbulence transport model, slip velocity, volume fraction equations being set at 0.1. The under relaxation factors for the k- $\epsilon$  turbulence transport model, density and body forces were set to 1.

The simulations were performed for 2000 time-steps with a step size of 0.1 seconds; to give 200 seconds of simulated flow time. After every time-step the vertical velocity of the liquid phase was recorded as an average of 16 points

across the width of the riser and 16 points across the width of each downcomer at heights 0.45 m from the base of the reactor. The gas phase holdup was recorded after each time step as an average with respect to the whole of the riser section of the column and for both of the downcomer sections.

### **Results and discussion:**

Figure 3 to Figure 6 present the vertical liquid phase velocity and the gas phase holdup for both the experimental and simulated results. Each of the simulated data curves is averaged with respect to space and then time. At each time-step an average value of the liquid velocity was recorded, this was a spatial average that comprised of the mean velocity of sixteen data points for the riser and sixteen points for each downcomer at a height of 0.45 m above the gas sparger. The gas phase holdup was obtained by averaging the all values in the riser and for the downcomer. From experimental data of both the circulation velocity and gas holdup it has been observed, that already 3-5 seconds from the beginning of each experiment these parameters became constant. Therefore these spatial averages were then averaged with respect to time, between 5 and 200 seconds of simulation time. For the experimental data a magnetically permeable particle was placed in the airlift reactor. As the particle travelled about the column with the liquid phase motion and as it passed through solenoid coils measuring an oscillation frequency, a change in this signal was observed. This change in signal appears as peaks, and the time difference in the peaks can be used to calculate the velocity of the gas-liquid mixture in both the riser and the downcomer. The series of peaks were used to produce a time-averaged velocity,

but as a particle rather than a point location was used the velocity is also averaged with respect to space. The gas holdup was determined by measuring the pressure difference across each section of the column (i.e. the riser and the downcomer) with manometers.

Figure 3 presents the vertical velocity in the riser for the experimental (■) and simulated data (△) against the superficial gas velocity in the riser. The trend of the experimental data is that of rapidly rising velocity up to  $0.02 \text{ m s}^{-1}$  of the superficial gas velocity in the riser. Then there is a reduction in the rate of change of the velocity as the turbulent flow effects begin to influence the gas phase motion for superficial gas velocity in the riser greater than  $0.02 \text{ m s}^{-1}$ . This change in the velocity profile is also observed in the simulated data at  $0.02 \text{ m s}^{-1}$  but more data points are required below this value to confirm the change. But generally the profile of the simulated data fits the empirical profile, except for the highest superficial gas velocity where a difference of greater than 15% or  $0.1 \text{ m s}^{-1}$  occurs.

The gas holdup in the riser is displayed in Figure 4 where comparisons of experimental (■) and simulated data (△) are made. The experimental gas holdup profile is linear with respect to the superficial gas velocity in the riser, suggesting that the slip of relative velocity between the gas and liquid phases does not change with increased gas through put. The gas fraction obtained from the simulated data over-predicts the empirical data, though the profile also has a linear form. The accuracy of the result is greater for the lower superficial gas velocities than at the high gas velocities.

The next figure presents the liquid phase velocity in the downcomer (Figure 5) and again the empirical data display two rates of change of velocity above and below  $0.02 \text{ m s}^{-1}$ . The flow regime changes as the influence of turbulent flow effects increase. The simulated data consistently over-predicts the liquid velocity and though the profile is not linear, more data is required for the lower range of superficial gas velocities is required to confirm this effect. The profiles in Figure 6 confirm this reduction in the accuracy of the flow data between the riser and downcomer where the gas holdup profiles are presented. Where a near linear change in the holdup is observed with the experimental data, the simulated data show comparatively little increase in the holdup of the downcomer for the majority of the superficial gas velocities. The only significant increases in the holdup in the downcomers occur at superficial gas velocities greater than  $0.05 \text{ m s}^{-1}$ . There are three effects in the model used that could influence the accuracy of the simulation in the downcomer, the use of a single gas fraction of a mean bubble size, the volume fraction equation formulation and the resolution of the mesh in the downcomer.

Figures 7-9 present the vector plots of the mixture phase from the numerical experiments. For this particular case the superficial gas velocity in the riser was  $0.02 \text{ m s}^{-1}$  and represent the state of the vector field after 200 seconds of simulation time. The dark shade vectors represent areas of low velocity for the fluid mixture. The highest numerically observed velocities were of the order of  $0.9 \text{ m s}^{-1}$  at the peaks of the meandering motion across the length riser. The oscillatory states were also visually observed experimentally.

For simplicity of the model and the exclusion of effects such as coalescence and bubble break-up, a single bubble size was used whereas a bi-modal bubble distribution occurs for high superficial gas velocities [12-15]. This effect can be observed in through the holdup in the downcomer and where very low superficial velocities lead to negligible gas holdup (less than  $0.01 \text{ m s}^{-1}$ ) as the driving forces increase the holdup increases as smaller bubbles are entrained in the downcomer flow. As smaller (less than 2 mm) are not modelled this effect is not observed in the simulation, but as the forces causing entrainment of the bubbles increase with increasing superficial gas velocity, the larger bubble become entrained. This is described by the small increases in the gas hold-up at superficial gas velocities greater than  $0.05 \text{ m s}^{-1}$ . Also the volume fraction equation used to model could influence how well the entrainment of gas bubbles in the downcomer fluids is modelled. The volume fraction equation is essentially a scalar equation modelling the transport of the gas phase fraction, looking at equation 3, there are three terms modelled. These are the change of fraction with respect to time, the convective transport of the gas phase and the inter-phase interaction term. This equation does not include terms such as diffusion and the deviatoric stress tensor that could incorporate entrainment of the gas phase bubbles into the downcomer fluids and therefore is not capturing an important part of the characterisation of airlift reactors. Finally the resolution of the mesh in the downcomer and at the regions where the fluid enters and leaves could also determine how well the gas phase entrainment is modelled here.

## **Conclusions:**

In the case of gas phase holdup and liquid phase velocities in the riser appropriate trends are followed and values are modelled to good accuracy, but the downcomer flow characterisation is poor due effects caused by the choice of the bubble size, volume fraction equation and mesh resolution used. Therefore to accurately model the motion of gas and liquid phases in airlift reactors, the use of complex multiple gas/discrete phase model equations must be implemented, where each discrete phase represents a single bubble size for the same gas phase composition. The inclusion of more than one gas phase will also lead to requirement of modelling bubble coalescence and break-up as this occurs in airlift reactors and this should be accompanied by a study of the bubble population in such reactors. Further investigations into the volume fraction equation used to model the gas phase transport are also required to assess how well the model equation captures bubble entrainment into the downcomer flows. It is also recommended that higher resolutions of the mesh in the region where there are large gradients in the velocity and the volume fraction of the gas phase, as this could inhibit gas phase transport.

*Acknowledgements. We would like to acknowledge the support of the Grant VEGA No. 1/0066/03 from the Slovak Scientific Grant Agency and Fluent Incorporated for enabling this work to be presented.*

## Nomenclature

### *General Symbols*

A	effect of system rotation of the Reynolds stress model
B	buoyancy effect term from Reynolds stress model
C	coefficient
$C'_1$	constant in the linear pressure-strain model, for the wall reflection term = 0.5
$C'_2$	constant in the linear pressure-strain model, for the wall reflection term = 0.3
$d_q$	bubble diameter (m)
$d_w$	distance to the wall (m)
F	external forces ( $\text{kg m s}^{-2}$ )
f	dimensionless friction factor (-)
G	generation of turbulent energy ( $\text{kg m}^{-1} \text{s}^{-3}$ )
g	acceleration due to gravity ( $\text{m s}^{-2}$ )
k	kinetic energy ( $\text{m}^2 \text{s}^{-2}$ )
n	unit normal vector (where the subscript defines the direction of the vector)
P	stress production term for the Reynolds Stress model
p	pressure shared by all phases ( $\text{N m}^{-2}$ )
Re	Reynolds number (-)
S	source term
t	time (s)
U	mean velocity ( $\text{m s}^{-1}$ )
u	velocity component ( $\text{m s}^{-1}$ )
v	slip velocity component ( $\text{m s}^{-1}$ )

x spatial co-ordinate (m)

### ***Greek Symbols***

$\alpha$  volume fraction

$\beta$  coefficient of thermal expansion

$\varepsilon$  rate of dissipation of turbulent energy ( $\text{m}^2 \text{s}^{-2}$ )

$\phi$  pressure strain

$\kappa$  constant for the linear pressure-strain model wall reflection term = 0.41

$\mu$  dynamic viscosity ( $\text{kg m}^{-1} \text{s}^{-1}$ )

$\rho$  density ( $\text{kg m}^{-3}$ )

$\Omega$  mean rate of rotation tensor

$\sigma_k$  turbulent Prandtl number for the kinetic energy = 1 (k- $\varepsilon$  turbulence transport) or 0.82 (Reynolds stress turbulence transport)

$\sigma_\varepsilon$  turbulent Prandtl number for the rate of dissipation of energy = 1.3

### ***Mathematical Operators***

D total differential operator

d differential operator

$\partial$  partial differential operator

$\Sigma$  summation

$\rightarrow$  vector form of variable (i.e. representing i, j and k forms of the variable as a matrix)

### ***Subscripts and Superscripts***

1	constant for the linear pressure-strain model = 1.8
2	constant for the linear pressure-strain model = 0.6
1 $\epsilon$	constant for the turbulent dissipation of energy = 1.44
2 $\epsilon$	constant for the turbulent dissipation of energy = 1.92
3 $\epsilon$	constant for the turbulent dissipation of energy
b	buoyancy
c	continuous phase
D <sub>p</sub>	drift velocity of the pth phase
i	co-ordinate index
j	co-ordinate index normal to i
k	kinetic energy
mix	mixture phase index
n	number of phases
q	phase index
r	co-ordinate index
s	co-ordinate index
t	turbulent
w	wall effects
$\mu$	turbulent viscosity constant = 0.09

## References:

1. Fluent Solvers, Fluent Europe Ltd, Sheffield Airport Business Park, Europa Link, Sheffield S9 1XU (www.fluent.co.uk)
2. J. Klein, O. Dolgoš, Š. Godó, M. Blažej, and J. Markoš, Application of a magnetic tracer method for the characterisation of hydrodynamics in internal-loop airlift bioreactors, *Chem. Pap.*, **54** (6b) (2000) 456-466.
3. G. M. Cartland Glover, S. C. Generalis, and N. H. Thomas, CFD and bubble column reactors: Simulation and experiment, *Chem. Pap.*, **54** 361-369 (2000)
4. G. M. Cartland Glover, S. C. Generalis, and N. H. Thomas, Dynamic simulations of multiphase flow in bubble columns, Chisa 2000, Poster G5.5, Prague, Czech Republic, 27-31 August (2000).
5. M. Y. Chisti, *Airlift Bioreactors*, Elsevier Science Publishers Ltd, New York, (1989).
6. M. Manninen, V. Taivassalo and S. Kallio, *On the mixture model for multiphase flow*, VTT Publications: 288, Espoo, Finland, (1996).
7. J. Sanyal, S. Vásquez, S. Roy, and M. P. Duduković, Numerical simulation of gas-liquid dynamics in cylindrical bubble column reactors, *Chem. Eng. Sci.*, **54** (1999) 5071-5083.
8. Fluent Inc., *Fluent 5 Users Guide*, Lebanon, New Hampshire, USA, (1998).
9. F. Kastánek, J. Zahradník, J. Kratochvil, J. Cermak, *Chemical Reactors for gas-liquid systems*, Ellis Horwood Limited, Chichester, England, (1993).

10. B. P. Leonard, A stable and accurate convective modelling procedure based on quadratic upstream interpolation, *Comp. Meth. Appl. Mech.*, **19** (1979) 59-98.
11. S. V. Patankar, *Numerical Heat Transfer and Fluid Flow*, McGraw-Hill, New York (1980).
12. G. Kuncová, and J. Zahradník, Gas holdup and bubble frequency in a bubble column reactor containing viscous saccharose solutions, *Chem. Eng. & Processing*, **34** (1995) 25-34.
13. J. Zahradník, M. Fialová, M. Ruzicka, J. Drahos, F. Kastánek, and N. H. Thomas, Duality of the gas-liquid flow regimes in bubble column reactors, *Chem. Eng. Sci.*, **52** (1997) 3811-3826.
14. J. Zahradník, G. Kuncová and M. Fialová, The effect of surface active additives on bubble coalescence and gas holdup in viscous aerated batches, *Chem. Eng. Sci.*, **54** (1999) 2401-2408.
15. M. Ruzicka, J. Drahos, J. Zahradník, and N. H. Thomas, Structure of gas pressure signal at two-orifice bubbling from a common plenum, *Chem. Eng. Sci.*, **55** (2000) 421-429.

**Table 1** Superficial gas phase velocity ( $\text{m s}^{-1}$ ) through the riser and through the sparger to enable comparisons between simulation and experiment. The sparger velocity is used defined the gas phase velocity in the simulations. Note that the gas flow rate corresponds to both the riser and sparger superficial gas velocities.

<b>Column section</b>	<b>Riser</b>	<b>Sparger</b>
<b>Cross-sectional area <math>\cdot 10^{-3}</math> (<math>\text{m}^2</math>)</b>	8.82	4.90
<b>Gas flow rate <math>\cdot 10^{-4}</math> (<math>\text{m s}^{-3}</math>)</b>	<b>Superficial gas velocity (<math>\text{m s}^{-1}</math>)</b>	<b>Superficial gas velocity (<math>\text{m s}^{-1}</math>)</b>
0.88	0.01	0.018
1.76	0.02	0.036
3.53	0.04	0.072
4.41	0.05	0.090
5.29	0.06	0.108
6.62	0.075	0.135

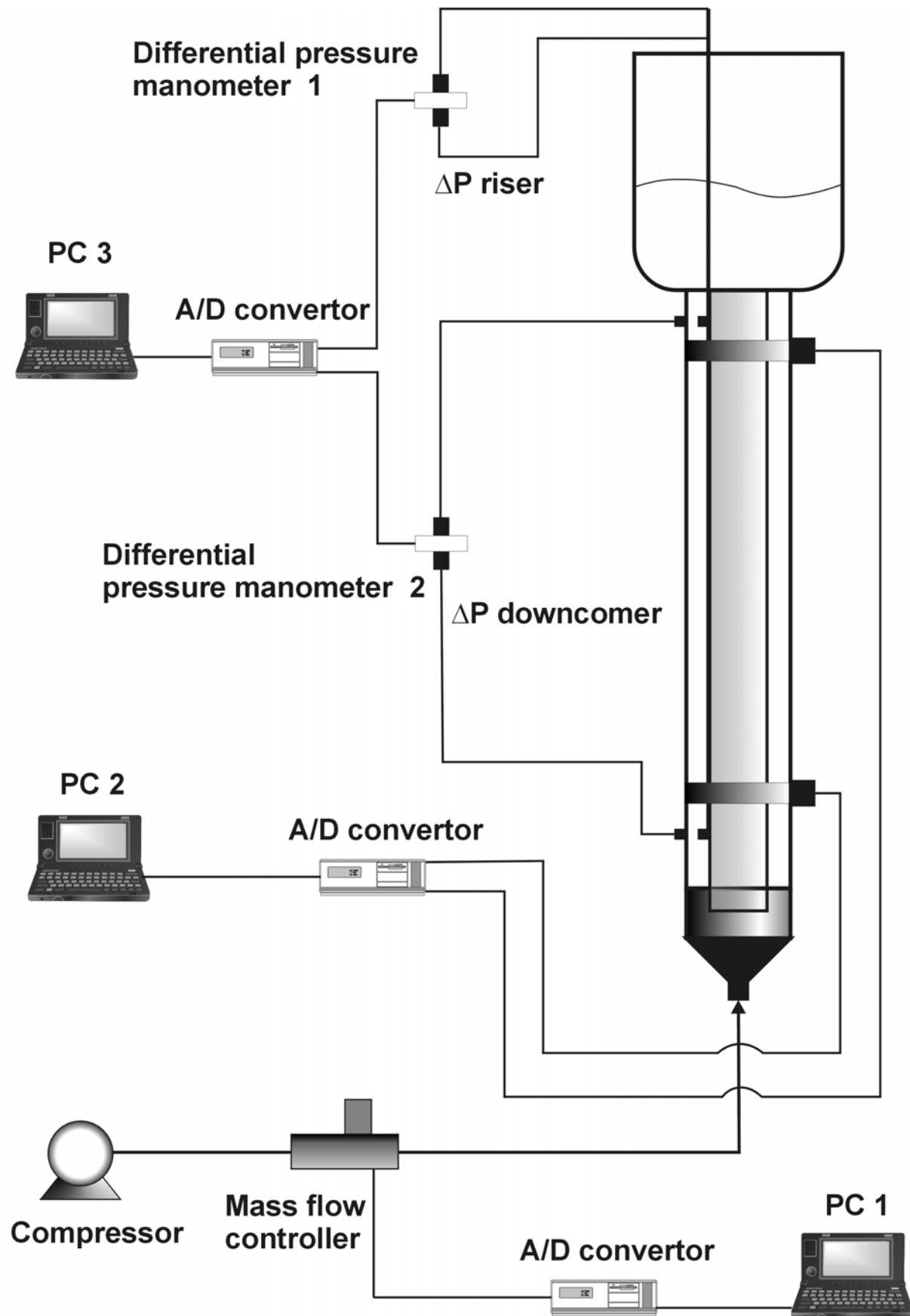
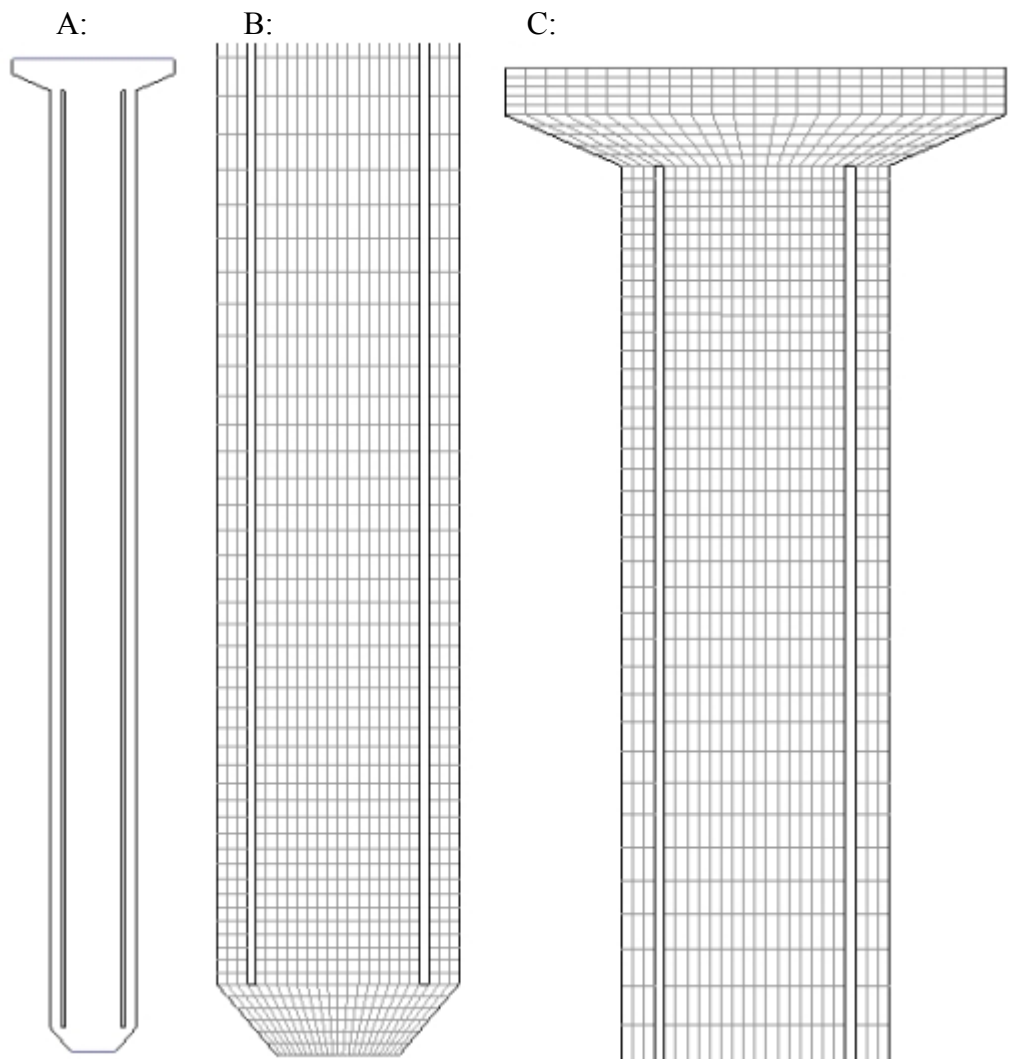


Figure1 Blažej et al., 2002



**Figure 2**      **Blažej et al., 2002**

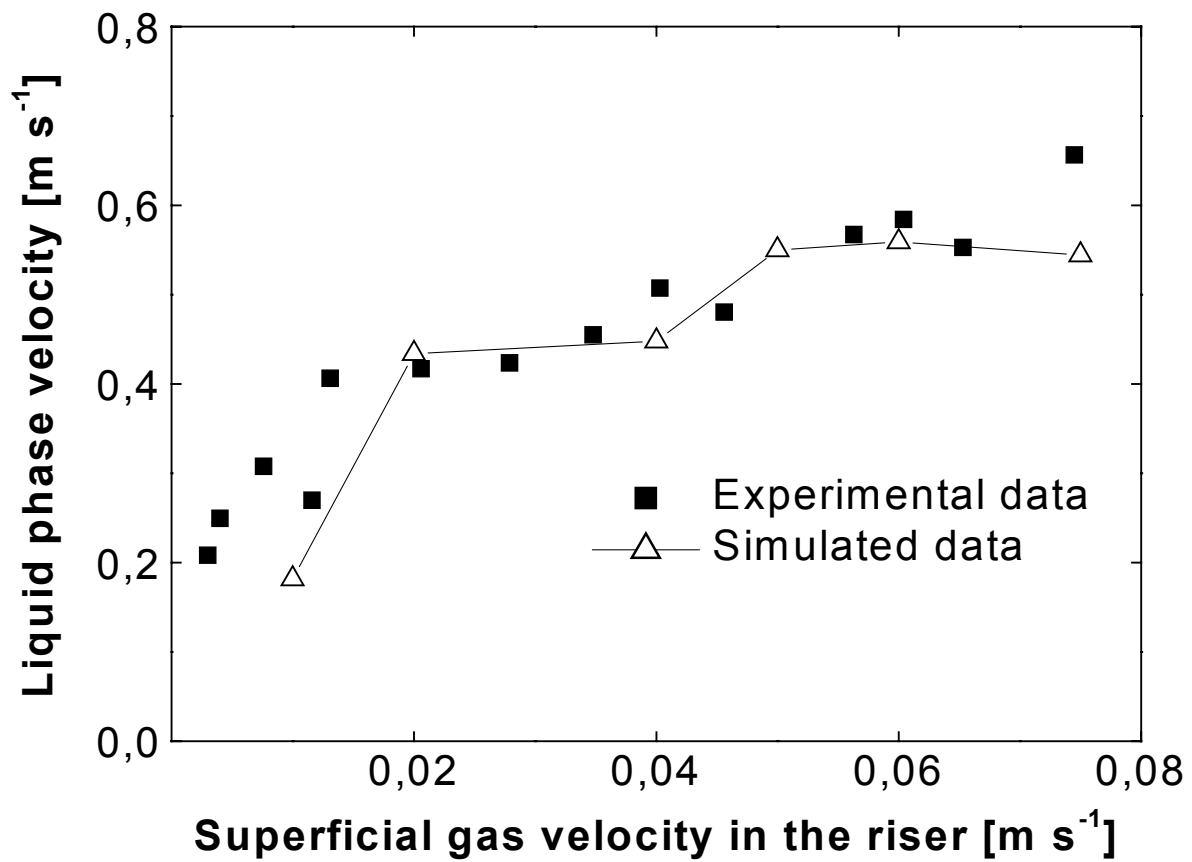


Figure 3 Blažej et al., 2002

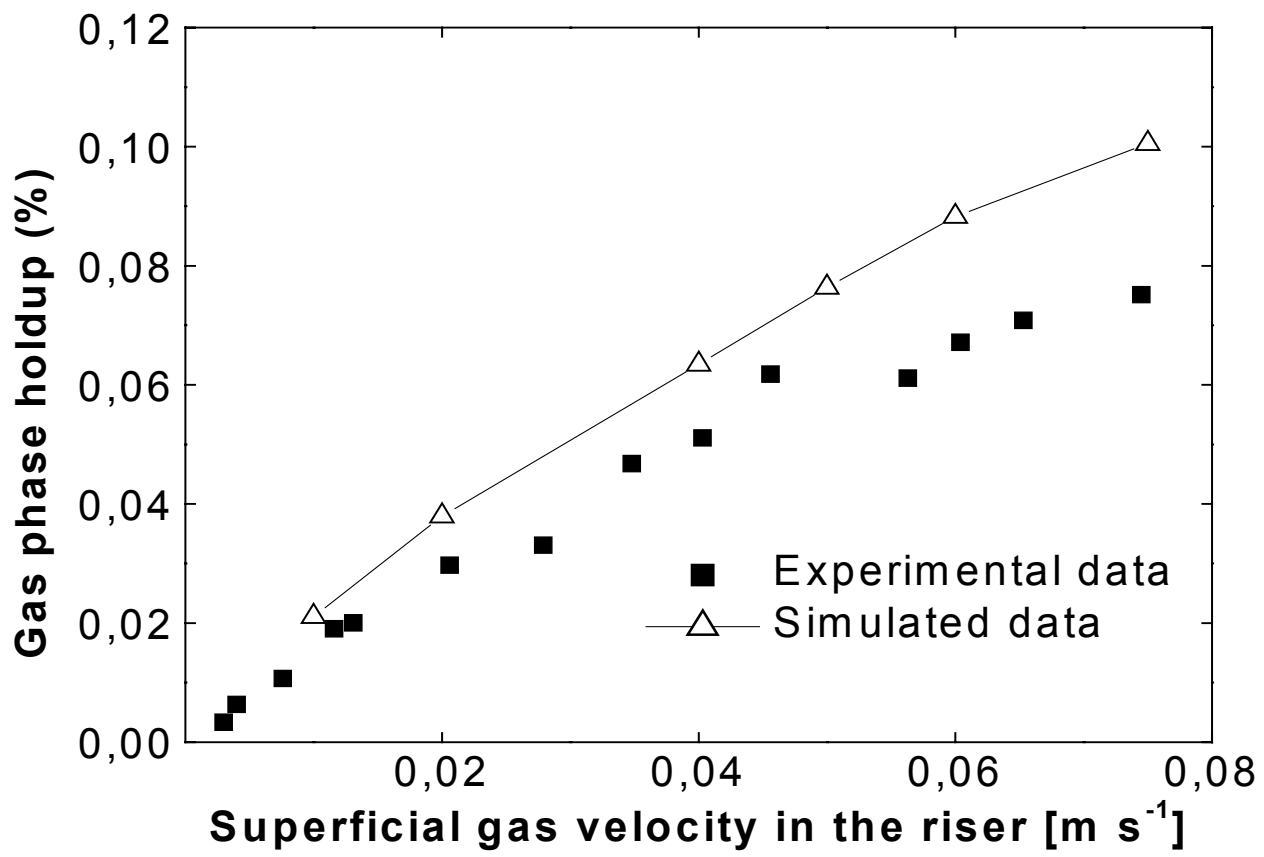


Figure 4 Blažej et al., 2002

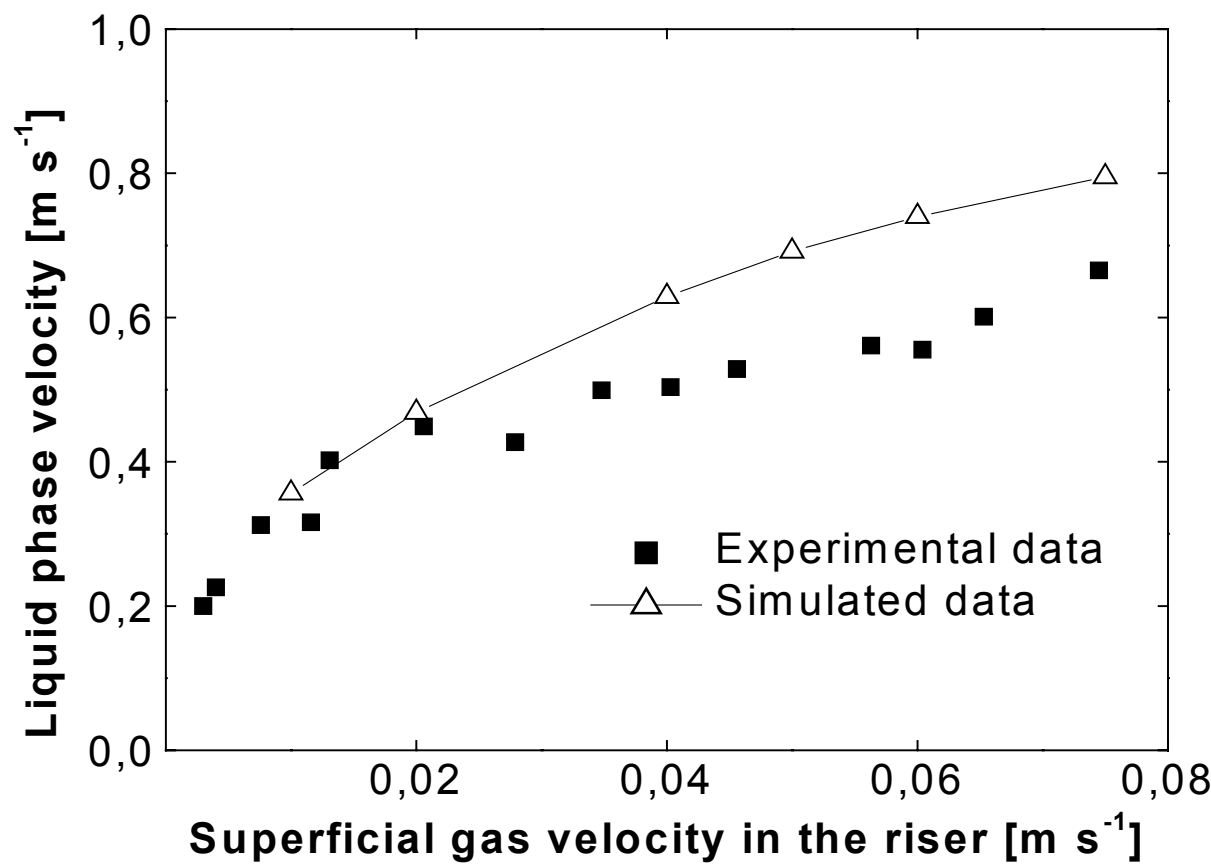


Figure 5 Blažej et al., 2002

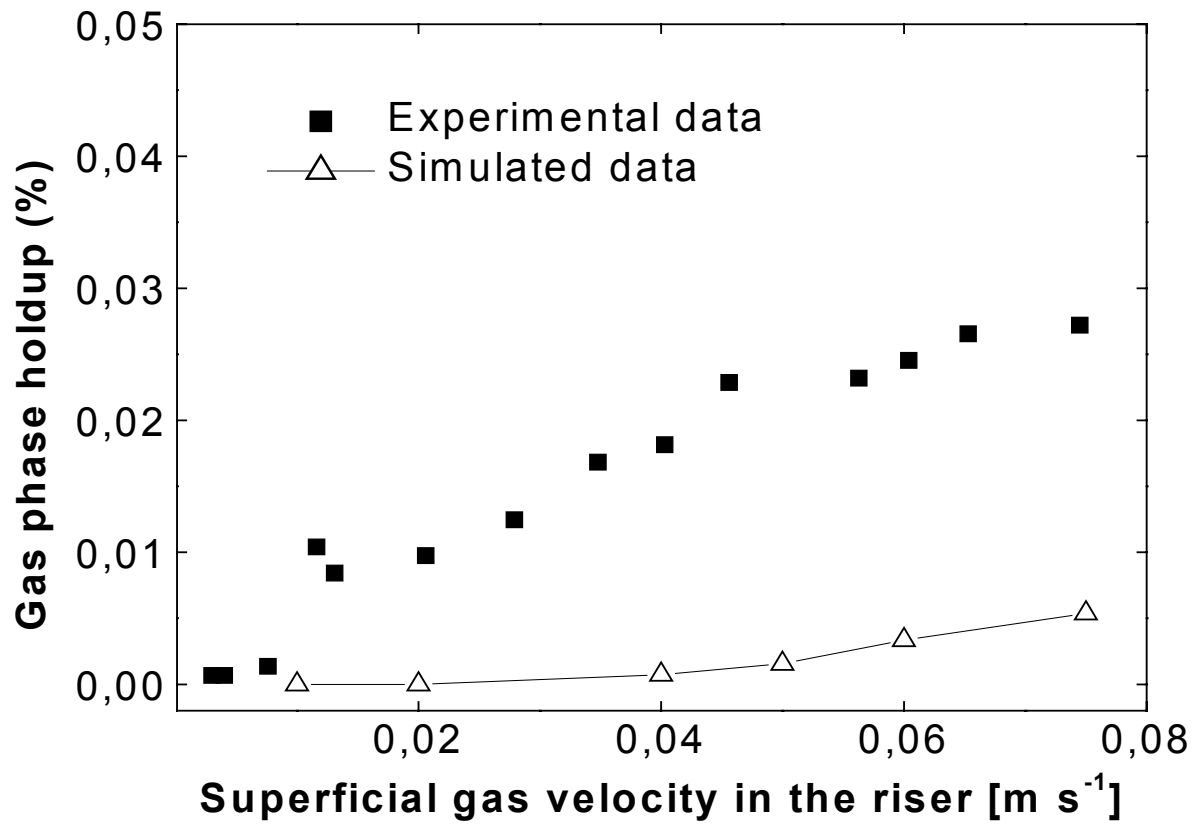


Figure 6 Blažej et al., 2002

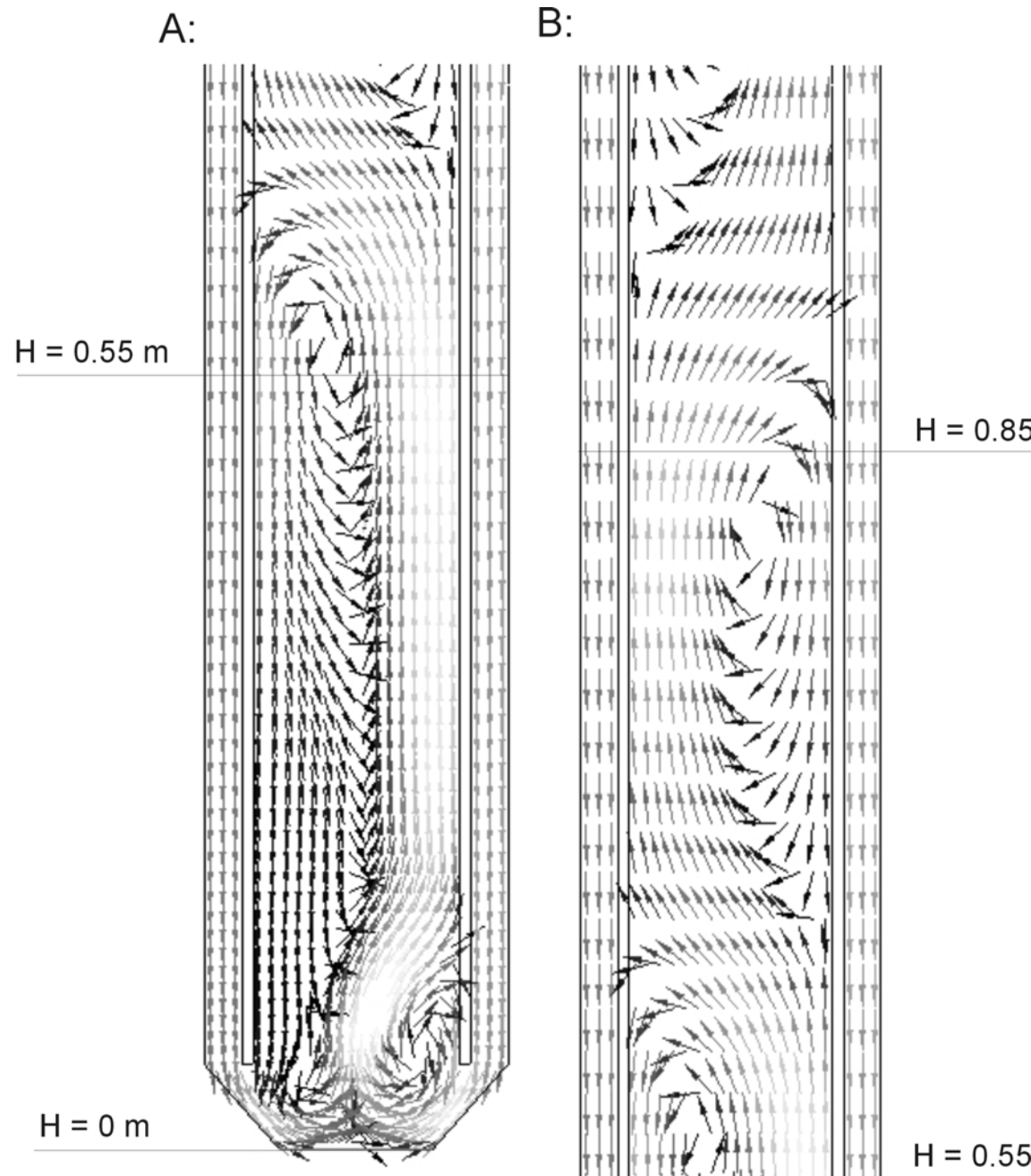


Figure 7 Blažej et al., 2002

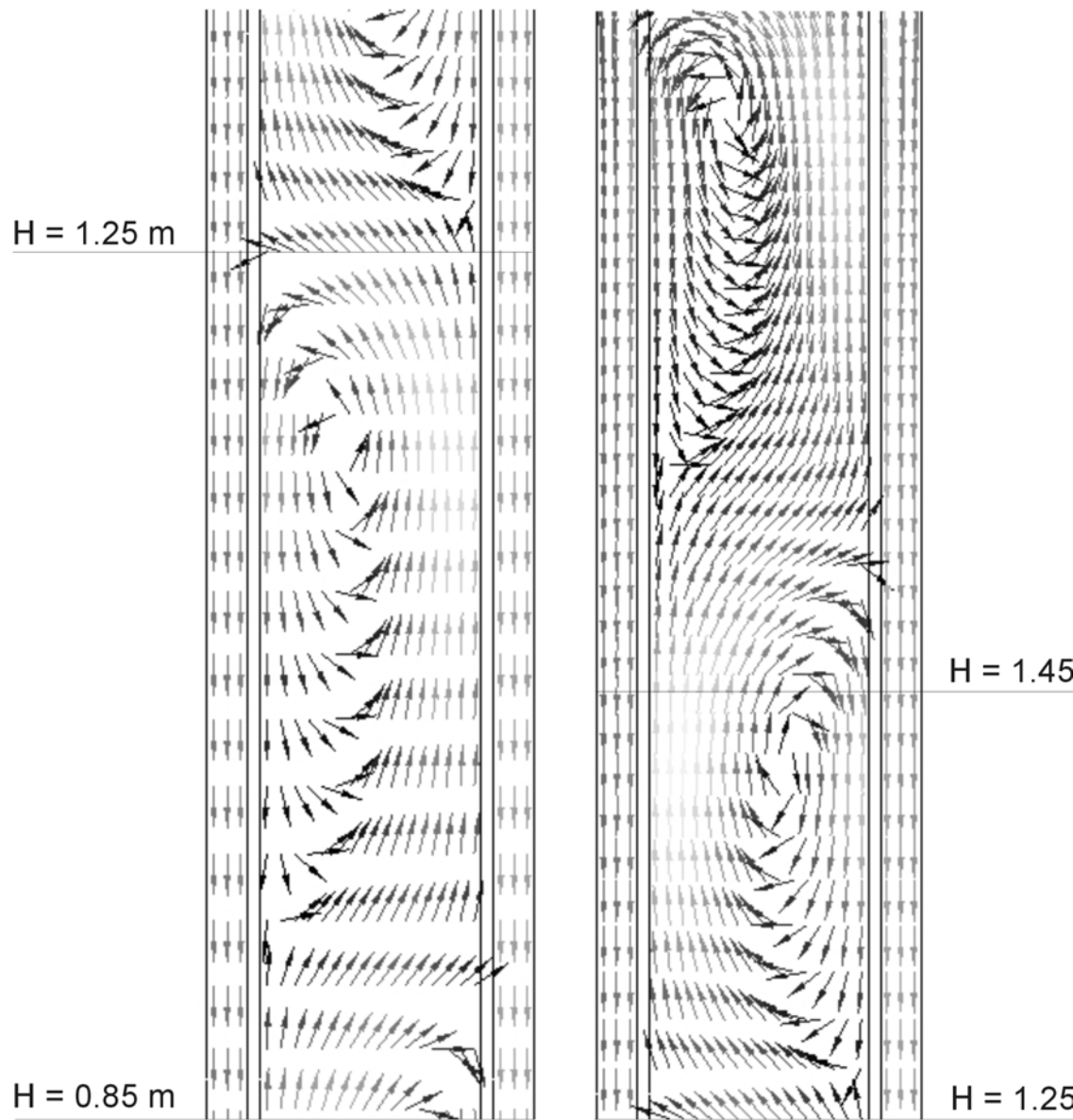
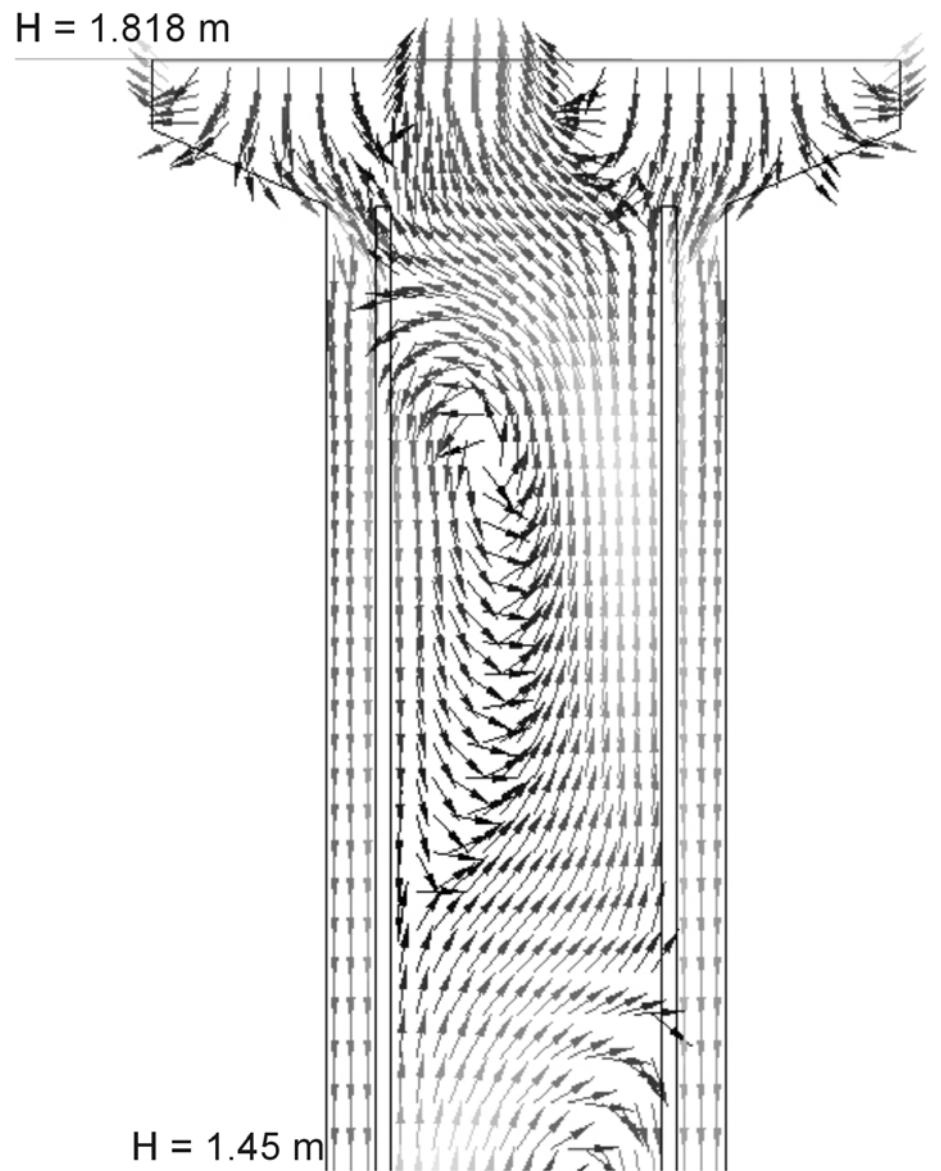


Figure 8 Blažej et al., 2002



**Figure 9** Blažej et al., 2002

**Captions for figures**

**Figure 1:** Scheme of the experimental equipment.

**Figure 2:** Diagram of the domain used to represent the airlift reactor in the simulation. A: The whole domain; B: The bottom of the reactor; C: The top of the reactor;

**Figure 3:** Liquid phase velocity ( $\text{m s}^{-1}$ ) in the riser as influenced by the superficial gas velocity in the riser ( $\text{m s}^{-1}$ ); ■: Experimental data collated from the magnetic particle; △: Simulated data obtained from Fluent;

**Figure 4:** Gas phase holdup (%) in the riser as influenced by the superficial gas velocity in the riser ( $\text{m s}^{-1}$ ); ■: Experimental data collated from the magnetic particle; △: Simulated data obtained from Fluent;

**Figure 5:** Liquid phase velocity ( $\text{m s}^{-1}$ ) in the downcomer as influenced by the superficial gas velocity in the riser ( $\text{m s}^{-1}$ ); ■: Experimental data collated from the magnetic particle; △: Simulated data obtained from Fluent;

**Figure 6:** Gas phase holdup (%) in the downcomer as influenced by the superficial gas velocity in the riser ( $\text{m s}^{-1}$ ); ■: Experimental data collated from the magnetic particle; △: Simulated data obtained from Fluent;

**Figure 7:** Vectors of velocity magnitude for the mixture phase ( $\text{m s}^{-1}$ ); A: Between 0 and 0.55 m above the base of the reactor; B: Between 0.55 and 0.85 m above the base of the reactor;

**Figure 8:** Vectors of velocity magnitude for the mixture phase ( $\text{m s}^{-1}$ ); A: Between 0.85 and 1.25 m above the base of the reactor; B: Between 1.25 and 1.7 m above the base of the reactor;

**Figure 9:** Vectors of velocity magnitude for the mixture phase ( $\text{m s}^{-1}$ ) between 1.45 and 1.818 m above the base of the reactor;